 CMC, vol.19, no.2, pp.199-216, 2010

# Effects of Loading Conditions on Deformation Process in Indentation

**M. Demiral, A. Roy and V. V. Silberschmidt**[1]

**Abstract:** Static indentation experiments are typically performed to characterize the mechanical properties of a material of interest by a rigid indenter of known geometry to various depths. In contrast, dynamic indentation of materials has not been fully studied. Evaluating material performance under dynamic loading conditions is a challenge and we demonstrate that various modelling schemes may be appropriate for different flavours of dynamic indentation. In order to compare underlying thermo-mechanics and deformation processes in a static and dynamic indentation process, indentation of a rigid indenter into a workpiece to a fixed chosen penetration is extensively studied. A nonlinear strain rate and temperature-sensitive material model is used to characterize the macroscopic response of a titanium-based beta-alloy to indentation.

**Keywords:** Static indentation, Dynamic indentation, Non-linear material behaviour, Finite element analysis

## 1 Introduction

Indentation has long been used as a technique for materials characterization. The measurements of applied load and the magnitude of the residual impression are used to determine the material hardness; this phenomenon is qualitatively related to the resistance to plastic deformation [Tabor (1950)]. Indentation experiments are also carried out to probe local properties, and potentially short- and long-range residual stresses at different size scales [Suresh and Giannakopoulos (1998)]. Therefore, parameters linked to stress and strain fields can be extracted by indentation. Residual stresses and strains provide information on the deformation behaviour of the material and the long-term response of components under service loads.

[1] Corresponding author. Tel.:+441509 +44/(0)1509/227504; fax: +44/(0)1509/227502. E-mail address: V.Silberschmidt@lboro.ac.uk

Although static indentation techniques, performed under quasi-static loading conditions, are helpful in determining material properties quite easily, their extension to dynamic loading conditions comparable to techniques such as the Split Hopkinson pressure bar [Kolsky (1949)] while maintaining simplicity is not fully established. Some of such attempts are known from the literature. For instance, Davis and Hunter (1960) used a conical indenter with an indenter speed ranging from 2 cm/s to 30 cm/s to study rate sensitivity of the material. The study of Mok and Duffy (1965) with spherical indenter's speed of up to 5 m/s revealed the deduced strain rate sensitivity; it can be roughly comparable to that evaluated using the Kolsky pressure bar technique. On the other hand, Tirupataiah and Sundararajan (1991) used a spherical ball as an impactor under high speeds (up to 180 m/s) to study the high-strain-rate flow behaviour of ductile metals and alloys. The general idea performing those experiments was to study the dynamic behaviour of engineering materials [Lu, Suresh and Ravichandrana (2003)].

Such experimental observations necessitate the numerical analysis of both static and dynamic indentations in order to evaluate the various deformation processes underlying these techniques. Different types of dynamic indentation scenarios are considered in this paper dependent on the inertial effects involved in the process. Understanding of such mechanism can also benefit comprehension of a material behaviour in machining processes such as turning, milling and drilling.

This is especially important for a relatively novel machining technique known as ultrasonically-assisted machining. The technique employs repetitive impacting with a low velocity and an amplitude of 10-20 $\mu$m. Such a transition from a traditional technique to a vibro-impact one enables machining of intractable materials by decreasing cutting forces [Ahmed, Mitrofanov, Babitsky and Silberschmidt (2007, 2009)], improving surface finish [Babitsky, Kalashnikov, Meadows and Wijesundara (2003)], reducing of tool wear and noise [Astashev and Babitsky (1998)] compared to conventional turning (CT). The chip formation process in ultrasonically-assisted turning (UAT) involves several physical processes such as large plastic deformation of the material inside the chip (which may be of the order of several hundred percent), friction of the chip and workpiece with tool at the rake and free face, respectively, complex interaction between the workpiece-chip-tool system itself [Astashev and Babitsky (1998)]. In order to gain a better understanding of the thermomechanics of this advanced machining technique, a separation (or even elimination) of some complicating features is necessary for a better understanding of underpinning deformational mechanisms. That leads us to consider the dynamic indentation process with a predefined indenter velocity as a process incorporating the main features of the real turning process but avoiding, e.g., effects due to its complex kinematics. In dynamic indentations such as used to analyse the

process of UAT, the movement of indenter is displacement controlled. On the other hand, a dynamic problem, in which the indentation process is not constrained and is fully detemined by the initial energy of the indenter and the materials properties of the imparted target is referred here as a 'fully dynamic process'.

## 2 Modelling consideration

To obtain a thorough understanding of different modelling regimes describing various scenarios, three different modelling schemes are considered to provide comparability of obtained numerical results. The indentation process for each modelling regime is studied for the same magnitude of the maximum penetration of the indenter into the target made of material under study.

First, we perform a static analysis (referred to as type A), without inertia effects-a scheme that have been traditionally used to simulate indentation tests. Two variants of dynamic analysis are studied, one with displacement control of the indenter's displacement, i.e., controlled dynamic analysis (type B). Another variant is a fully dynamic analysis, in which the deformation process is governed by the initial velocity of the indenter and the target's properties (type C).

The displacement-controlled dynamic analysis (type B) is divided into three subtypes, corresponding to different velocities of the indenter to study its effect on the overall deformation behaviour. First we consider a low-velocity indenter motion. This scheme (subtype B1) is a better representation of real physical indentation tests than type A. Subtype B2 models the effects of indenter velocity of 10 m/s is linked to the relative velocity between the cutting tool and workpiece in UAT to study the deformation process of UAT [Ahmed, Mitrofanov, Babitsky and Silberschmidt (2007; 2009)]. The level of indentation velocity in subtype B3 is linked to that in type C, so that these two regimes could be compared. As the indenter displacement is not controlled in type C, the magnitude of initial velocity was obtained iteratively to get the same level of the maximum penetration into the target in types A and B for different contact conditions; the same level is used in subtype B3. A summary of various indenters' velocities used for the various modelling scenarios is listed in Tab. 1.

## 3 Finite-element modelling of indentation

A two-dimensional finite-element (FE) approximation of an indentation process (Fig. 1) is modelled using the FE software package *MSC.Marc* [MSC, Marc User's Guide (2008)]. In physical indentation tests heat is generated due to plastic deformation and the work done to overcome the frictional forces between the indenter and workpiece. This leads to the generation of thermal strains and volumetric ex-

Table 1: Different indentation modelling regimes

| Types and Subtypes | | Problem |
|---|---|---|
| Type A | | Static |
| Type B | Subtype B1 | Controlled dynamic, $V$= 0.001 m/s |
| | Subtype B2 | Controlled dynamic, $V$= 10 m/s |
| | Subtype B3 | Controlled dynamic, $V$= 1785 m/s ($\mu$ =0), $V$= 2000 m/s ($\mu$ =0.8) |
| Type C | | Fully dynamic, initial $V$= 1785 m/s ($\mu$ =0), initial $V$= 2000 m/s ($\mu$ =0.8) |

pansion, which in turn affects the mechanical response of the workpiece material. For these reasons our FE model is fully thermomechanically coupled.

The chosen dimensions of the workpiece are 40 mm in width and 10 mm in height (Fig. 1). Our preliminary numerical simulations demonstrated that these dimensions are sufficiently large to be insensitive to the effects due to traction-free boundary conditions on the indentation results.

Initially, a coarse mesh of 600 four-noded, isoparametric, quadrilateral heat transfer elements is used to discretize the workpiece (Fig. 1). Since the finite elements in the deformation zone under indenter are highly distorted in the indentation process causing numerical convergence problems and, in some cases, preliminary termination of the analysis, two automatic remeshing zones (zone_1 and zone_2, Fig. 1) are defined, with average element sizes of 20 $\mu$m and 1000 $\mu$m, respectively. Kinematic boundary conditions are imposed on the bottom face of the workpiece by constraining displacements in both $x$- and $y$-directions (Fig. 1), whereas the top, left, and right faces are free to deform.

The indenter is considerably stiffer than the workpiece under study and is modelled as a rigid body with a density of $\rho$=15000 kg/m$^3$. Triangular elements of an average size of 100 $\mu$m are used to discretize the indenter, which has an overall area of 1.706 mm$^2$. A relative movement of the workpiece and indenter is introduced as translation with a prescribed velocity in the negative $y$-direction for cases A and B. The indenter penetrates 0.5 mm of the workpiece, at the completion of which the indenter immediately retracts back to its original position. The velocities of indenter during the indentation are 1 mm/s, 10000 mm/s and 178500 mm/s (Tab. 1) for the idealized contact condition in analysis types B1, B2 and B3, respectively. The motion of indenter for type C analysis is controlled by an initial velocity value of 178500 mm/s for frictionless contact conditions.

The indenter angle value of $\varphi = 45^\circ$ with a circular curvature of 0.1 mm radius at

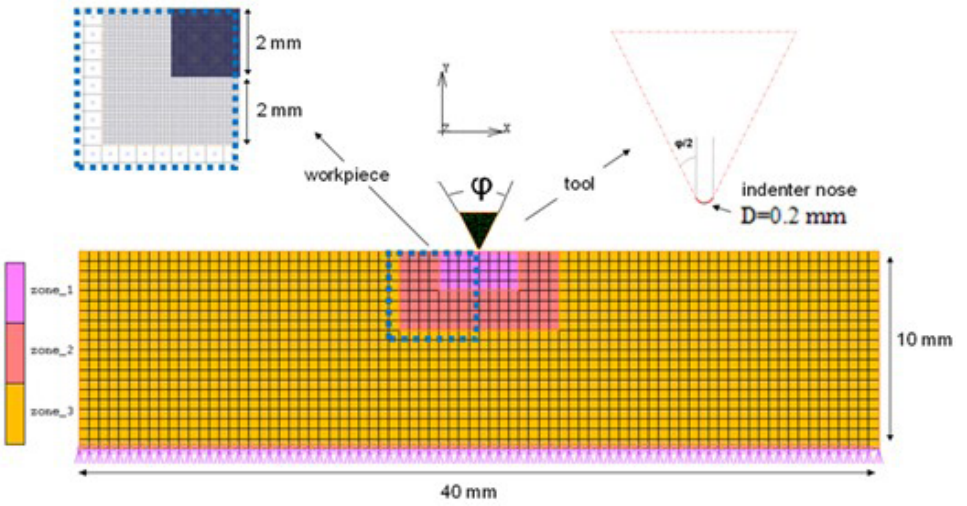


Figure 1: Mesh and boundary conditions used in FE simulations together with enlarged images of indenter and fine-meshed zone

its tip (Fig. 1) is considered in this study [Demiral, Roy and Silberschmidt (2010)]. The selected angle is within the limits for standard wedge indenters [Nanoindenters (2010)] as well as cutting tools typically used in UAT.

### *3.1 Material model*

A material for the target (indented workpiece) is a Ti-based superalloy (Ti15V3Cr3-Al3Sn) used in our UAT studies. In order to obtain a stress-strain behaviour of this alloy under various strain rates ($\dot{\varepsilon}$) and temperatures, a split-Hopkinson test [Li and Lambros (1999)] was carried out at Tampere University, Finland. The specimen used in the test was 8 mm in diameter and 8 mm in length. Figure 2 shows the material response of the alloy for different strain rates obtained in the test. The material properties of the alloy are $E$=87 GPa, $\nu$=0.3, $\rho$=4900 kg/m$^3$, where $E$, $\nu$ and $\rho$ are the Young's modulus, Poisson's ratio and density of the material, respectively. Experimental results characterizing the temperature-dependent thermal expansion coefficient [Material property data (2010)] and specific heat value of the workpiece material ($C_P$) used in the simulations are shown in Figs. 3 and 4, respectively. Specific heat has been measured in the temperature range between room temperature and 1200˚C by means of differential scanning calorimetry (Netzsch DSC 404) calibrated by a sapphire standard [Blumm and Kaisersberger (2001)].The conductivity of Ti alloy is $k$=8.08 W/m.K. The nonlinear strain-rate and temperature-sensitive material model used in our numerical simulations con-

sists of sixteen different stress-strain curves obtained for a combination of four different strain rates ($\dot{\varepsilon}$=0.1 $s^{-1}$, 1 $s^{-1}$, 3331 $s^{-1}$, $10^{10}$ $s^{-1}$) and four different temperature values (20˚C, 600˚C, 800˚C, 940˚C). These curves are modified in such a way that the magnitude of stress values for high strain values are limited by the ultimate dynamic tensile stress (UTS) [Ng, El-Wardany, Dumitrescu and Elbestawi (2002), Maudlin and Stout (1996)] (Figs. 5, 6). As the highest strain rate obtained from the Split-Hopkinson tests $\dot{\varepsilon}$=3331 $s^{-1}$was the stress-strain data for very large strain rate value ($\dot{\varepsilon}$=$10^{10}$ $s^{-1}$) was taken with a 20% offset from the corresponding values for $\dot{\varepsilon}$=3331 $s^{-1}$ (Fig. 5).

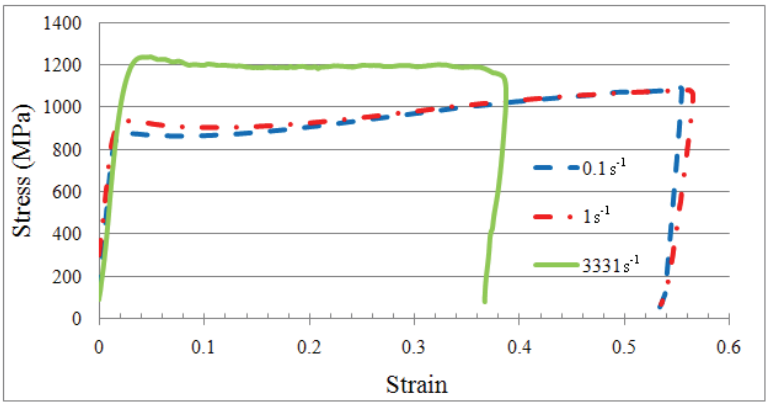


Figure 2: Stress-strain diagrams of Ti15V3Cr3Al3Sn obtained from split-Hopkinson test for different strain rates at room temperature (20˚C).

### *3.2 Friction model*

The classical Coulomb model, with the friction force being a linear function of normal force can predict unrealistically high forces at the indenter-workpiece interfaces at velocities corresponding to the UAT regime [Mitrofanov, Ahmed, Babitsky and Silberschmidt (2005)] and hence is not used in our model. On the other hand, the shear friction model, in which the friction force depends on a fraction of the equivalent stress of the material, is known to better represent the friction process and thus adopted in our study. The friction stress $\sigma_{\text{fr}}$ is introduced in the following form [MSC, Marc User's Guide (2008)]:

$$\sigma_{\text{fr}} \leq -\mu \frac{\bar{\sigma}}{\sqrt{3}} \frac{2}{\pi} \text{sgn}(v_r) \arctan(\frac{v_r}{v_c}) ,$$

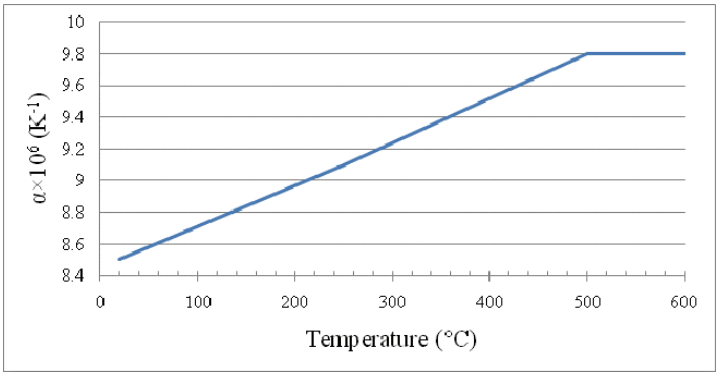


Figure 3: Thermal expansion coefficient of Ti15V3Cr3Al3Sn for different temperatures

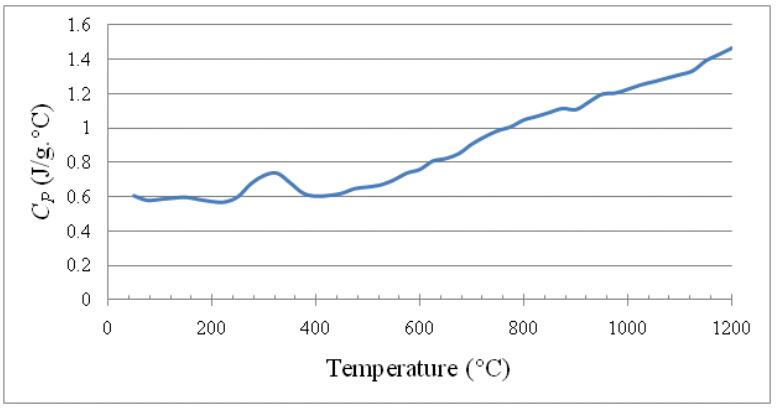


Figure 4: Specific heat of Ti15V3Cr3Al3Sn obtained from differential scanning calorimetry (Netzsch DSC 404)

where $\bar{\sigma}$ is the equivalent stress, $v_r$ is a relative sliding velocity, $v_c$ is a critical sliding velocity below which sticking is simulated, $\mu$ is a friction coefficient, and sgn() gives the sign of the argument . Two different values of the friction coefficients - $\mu$=0.0 and $\mu$=0.8 - are used in the simulations. Needless to say, $\mu$=0.0 accounts for the idealized frictionless condition, considered as an extreme case of friction reduction due to perfect lubrication, and $\mu$=0.8 accounts for a case of high friction, e.g., due to a lack of lubrication (dry condition).

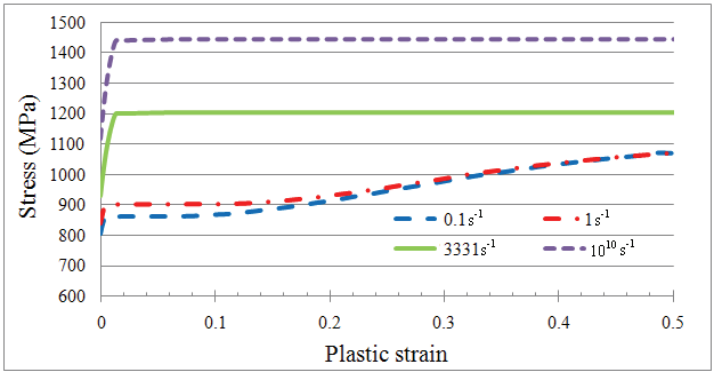


Figure 5: Modified strainrate-sensitive material model for 20˚C

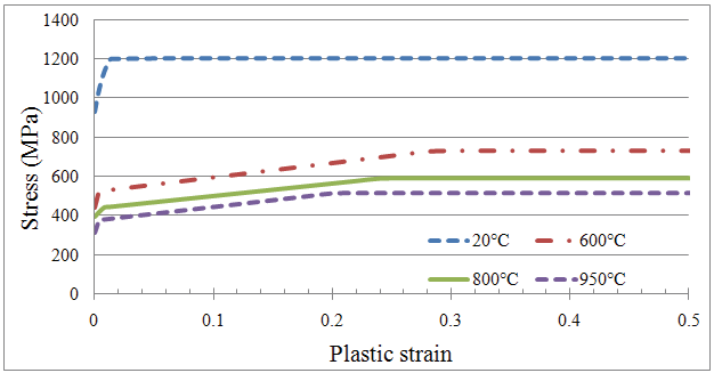


Figure 6: Modified temperature-sensitive material model for $\dot{\varepsilon}$=3331 $s^{-1}$

## 4 Numerical results and discussion

In this section the numerical results of different modelling regimes are evaluated in terms of reaction force, pile-up height, stress and temperature distribution to compare and contrast various experimental scenarios.

### *4.1 Reaction force*

The force-displacement diagram (Fig. 7), which can be obtained experimentally, is used to compare the deformation process in the workpiece for different modelling schemes. The area under this diagram is the energy expended, linked to the relative deformation level of workpiece for different analyses. Figure 7 shows the force-displacement diagrams for various cases studied.

Type A and subtype B1 have similar force-displacement behaviours, whereas the amount of energy dissipated increases with an increasing velocity of the indenter. Type B3 exhausts the most energy among the analyses followed by type B2 as expected. On the other hand, type C has a unique characteristic of force-displacement behaviour compared to the others. In a fully dynamic simulation, the indenter penetrates the workpiece solely thanks to initial inertial energy. However, with an increasing penetration after reaching some depth (approx. 0.35 mm for conditions modelled in case C) the force imposed by the indenter (consequently, the reaction force) decreases due to the work done by the process. Eventually, the indenter decelerates to a complete stop before recoiling off the workpiece surface.

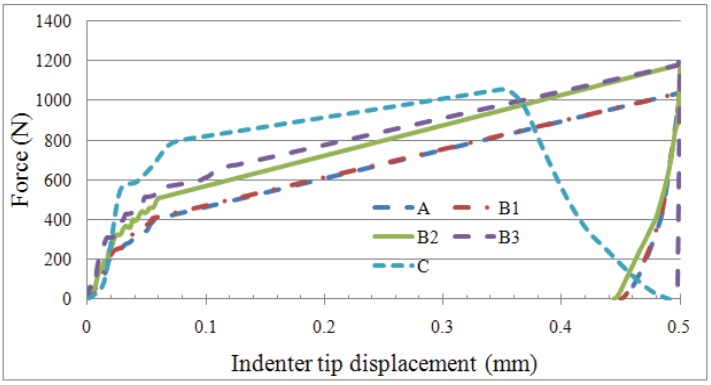


Figure 7: Force-displacement diagrams for various indentation models ($\mu$=0.0)

It is also observed that the reaction force at the maximum indentation depth increases as the coefficient of friction between the indenter and workpiece increases (Fig. 8). This is because the indenter expends more energy to overcome the frictional forces due to dry contact conditions in contrast to a well-lubricated indenter-workpiece interface. The additional heat caused by friction leads to an elevated temperature profile in the workpiece due to the indentation process in comparison to frictionless conditions as shown in Fig. 9. The respective temperature increase can reach 135˚C (Fig. 9) for subtype B3.

### *4.2 Pile-up height*

It is well known that an indentation process leads to a formation of a ‘pile-up’, an upward extrusion of displaced workpiece, which forms a raised crater [Garrido Maneiro and Rodriquez (2005)] on the surface of the workpiece. With an increase in the friction coefficient, it is expected that the relative motion (displacement)

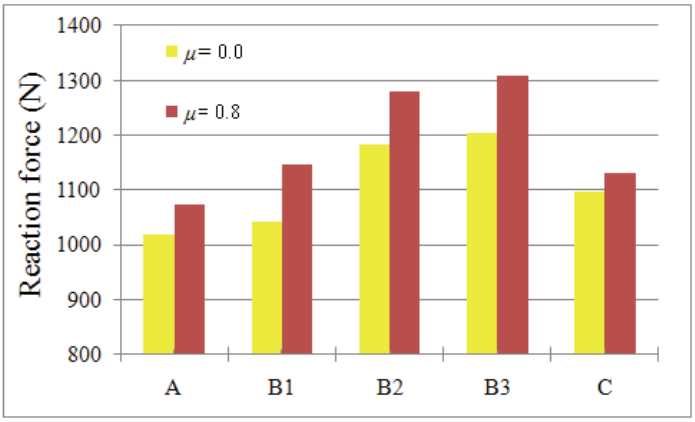


Figure 8: Reaction force magnitudes at maximum penetration for different modelling schemes and contact conditions

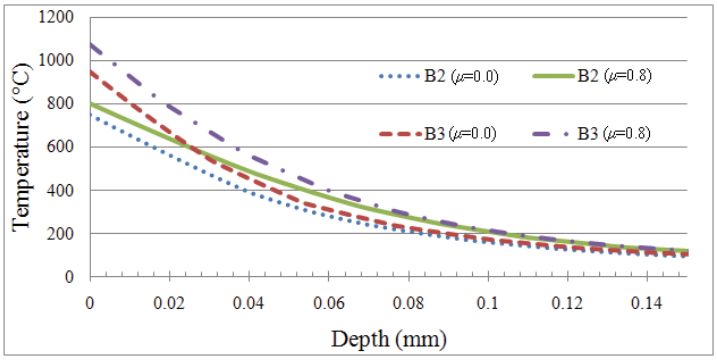


Figure 9: Temperature distribution along vertical depth (line AB in fig. 10) on deformed workpiece configuration at maximum penetration for controlled dynamic analysis under different contact conditions

between the indenter surface and the workpiece material will be increasingly hindered during the indentation process. In order to quantify the pile-up formation, we measure the its height $h$, which is the displacement of pile-up tip with respect to the undeformed surface in the direction parallel to indenter motion as shown in Fig. 10. The values obtained in our numerical experiments are summarized in Fig. 11; an increase in pile-up height is observed with increasing lubrication of the workpiece-indenter interface. The results are in good agreement with observed results in the literature [Garrido Maneiro and Rodriquez (2005)].

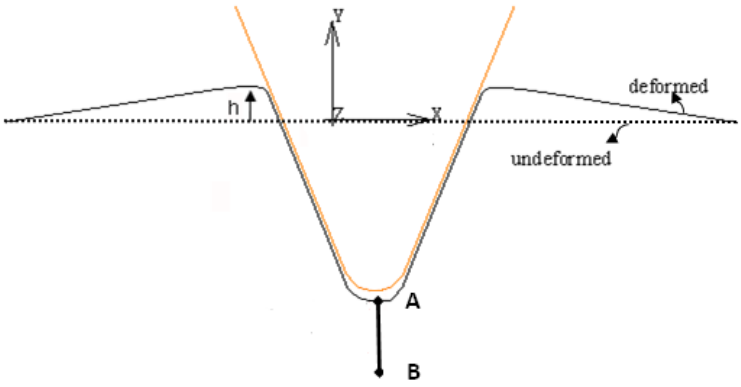


Figure 10: Scheme of pile-up around indenter. Points A and B denotes the distance travel by the indenter during indentation

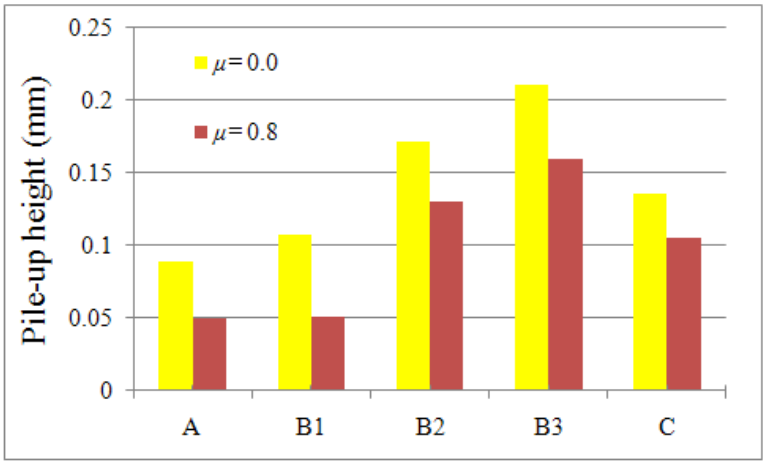


Figure 11: Spatial location of pile-up's tip with respect to undeformed surface for different modelling schemes and friction coefficients

### *4.3 Stress and temperature distributions*

The stress distribution in the area where the indenter penetrates the workpiece (zone_1, Fig. 1) was studied; this is the zone of high stress concentration. In order to quantify the extent of strongly affected zone, the workpiece area (or, rather its half due to symmetry) with von Mises stresses exceeding 500 MPa is used (Fig. 12). Since the inertial effects of indenter on the overall stress distribution in the

workpiece increase as the indentation velocity grows, subtype B3 has the largest critical area (2.42 $mm^2$), followed by subtype B2 (2.26 $mm^2$) and type C (1.97 $mm^2$). On the other hand, the influence of indenter inertial effects in the controlled dynamic process with velocity value of 1 mm/s (subtype B1) is lower than in other dynamic processes and comparable with that of type A (Fig. 12).

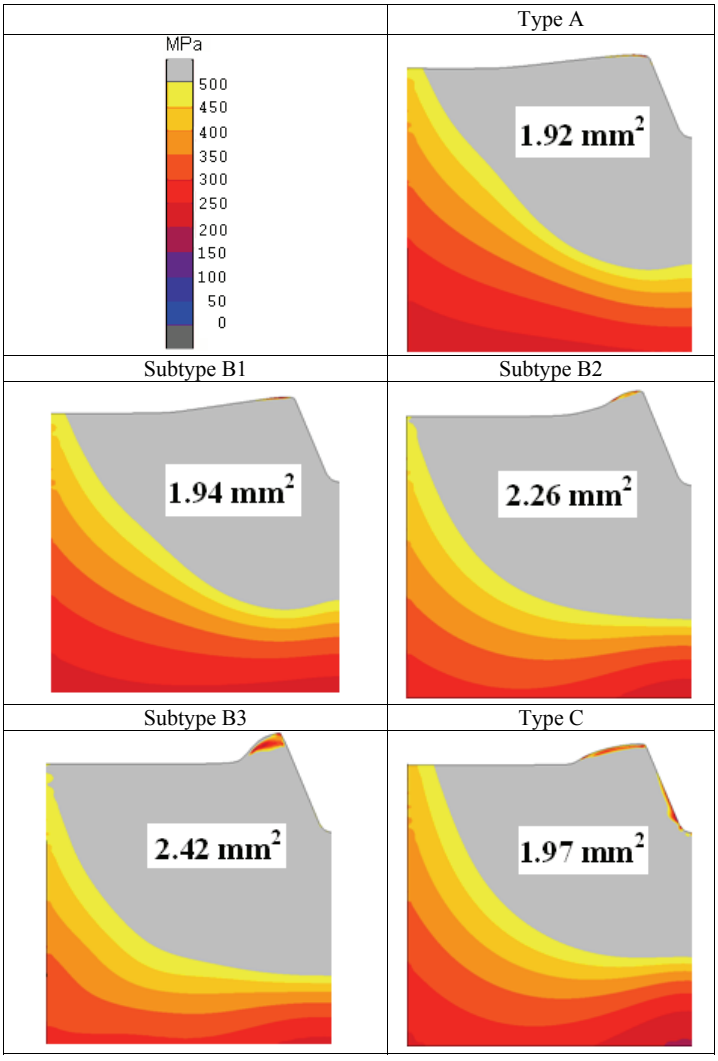


Figure 12: Von Mises stress distribution near indenter at maximum penetration for different modelling schemes ($\mu$=0.0)

The effects of different modelling paradigms on the predicted residual stresses are also studied. These stresses remain in the material when all external loads are removed and are superimposed with stresses subsequently applied to a structure or its components. The residual stresses are difficult to measure, hard to model and their distribution is not immediately apparent. In a machined layer, they are induced due to high deformation and temperature levels in the machining region and are an important feature of any metal-cutting operation [Ahmed, Mitrofanov, Babitsky and Silberschmidt (2006)]. In the case of compressive residual stresses introduced in any thermomechanical process, the fatigue and corrosion life of the produced component significantly increases, whereas tensile residual stresses may reduce the performance or cause failure of manufactured products, increase the rate of damage by fatigue, creep, or environmental degradation [Bocciarelli and Maier (2007)]. Therefore, the compressive and tensile components of residual stresses induced have different effects on the subsequent deformation process of the workpiece. For example, the residual stress values of $\sigma_{11}$ = -108 MPa and $\sigma_{11}$ = -132 MPa were obtained at a distance of 1 mm in vertical direction from the indenter tip under dry contact conditions for type A and subtype B1, respectively, whereas the subtype B3 and type C have tensile residual stress values at the same location with subtype B2 having a nearly vanishing stress level (Fig. 13). These results demonstrate that different loading types may lead to completely different effects on the deformation process for the same mechanical process being characterized. For a repetitive indentation process, which is an inherent feature of UAT, the signs and magnitudes of the residual stresses after each penetration play an important role in realization of the deformation process for subsequent indentations. In other words, the leading deformation process of indentation is influenced by residual stress distribution of the workpiece from the previous indentation.

The von Mises stress distribution at the maximum depth of indentation for dry contact condition (Fig. 14) elucidates the effects of two main parameters, strain rate and temperature, affecting the stress values in the vicinity of the indenter tip. The von Mises stress values are highest in static analysis followed by the controlled dynamic analyses, decreasing with growing velocity of the indenter as seen in Fig. 14. These observed results may be explained by material model used for Ti-15-3-3-3 (Figs. 5 and 6). The stress-strain curves obtained from the experiments demonstrate strain rate hardening of the alloy. But this process can be compensated by thermal softening of the material, is also observed with increasing temperature. Figure 15 shows that the temperature values for type C and subtypes B2 and B3 are much larger than those of other schemes, thus causing lower stress values at the indenter tip, though these areas typically experience higher strain rates (Tab. 2) which could have led to higher stress magnitudes. This shows that the effect of temperature

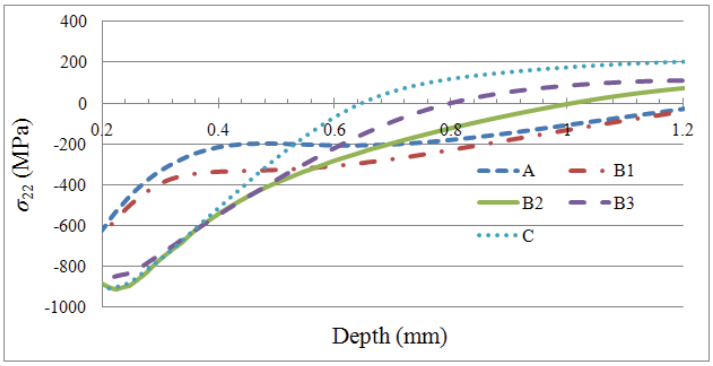


Figure 13: Distribution of residual stress $\sigma_{11}$ along depth (line AB in Fig. 10) on deformed workpiece configuration for different modelling schemes ($\mu$=0.8)

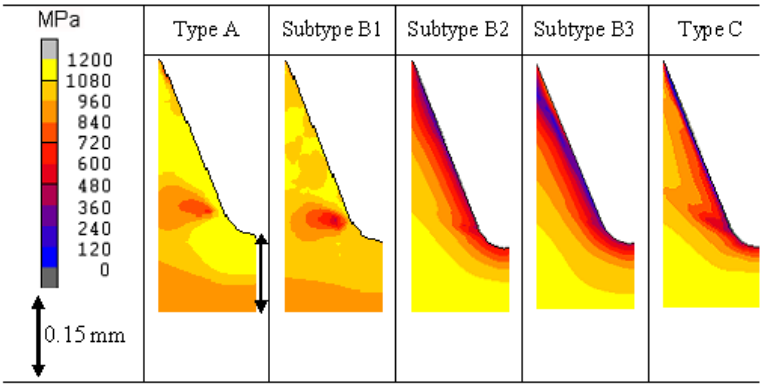


Figure 14: Distribution of von Mises stresses on deformed workpiece configuration for different modelling schemes at maximum penetration ($\mu$=0.8)

softening outweighs the effect of strain-rate hardening in the location close to the indenter tip. However, it is believed that the latter factor is more prominent in areas away from the indent. This can explain lower von Mises stress values for type A and subtype B1 in these areas (Fig. 14).

A close examination of temperature distributions for static (type A) and quasi-static analyses (subtype B1) (Fig. 16), demonstrates that the temperature values are larger for a latter case. This is due to the inertial effects of indenter on the numerical results. Still, there is a gradient in temperature distribution for the former case, though the solution has no time dependency. This demonstrates the transient characteristic of the indentation process.

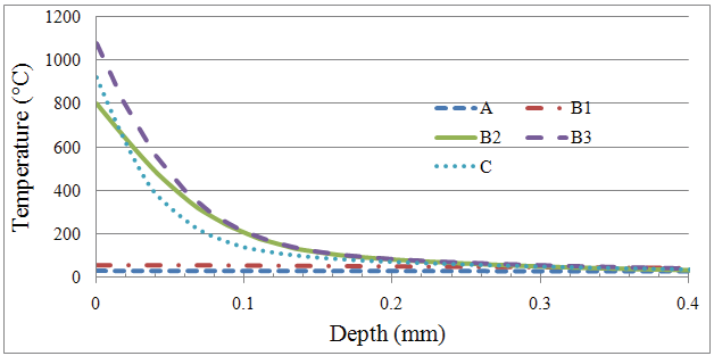


Figure 15: Temperature distribution along vertical depth (line AB in Fig. 10) on deformed workpiece configuration at maximum penetration for different modelling schemes ($\mu$=0.8)

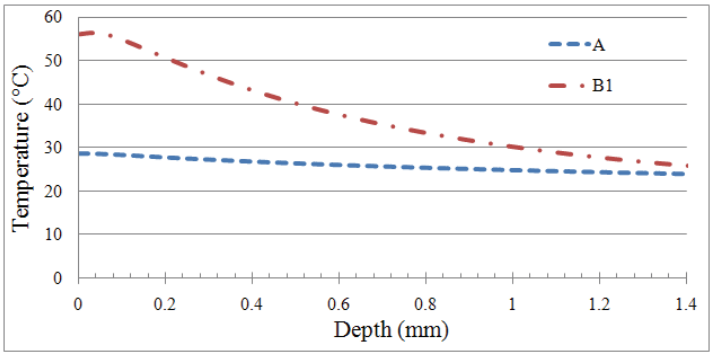


Figure 16: Temperature distribution along penetration vertical depth (line AB in Fig. 10) on deformed workpiece configuration at maximum penetration for type A and subtype B1 ($\mu$=0.8)

Table 2: Average strain rate values in workpiece (near indenter tip) at maximum penetration for different modelling schemes ($\mu$=0.8)

| Type or subtype | A | B1 | B2 | B3 | C |
|---|---|---|---|---|---|
| Strain rate ($s^{-1}$) | 0 | 1 | $10^5$ | $10^6$ | $10^3$ |

## 5 Conclusions

2D thermomechanically coupled FE approach is used to study different modelling paradigms in order to gain a clear understanding of the underlying deformation

mechanisms for the indentation problem studied. In contrast to time-independent static analysis, inertial effects are included in dynamic analyses to characterize the transient deformation processes associated with dynamic impacts.

The obtained results for the force-displacement diagram and indenter reaction force indicate that with an increasing indenter velocity, the inertial effects begin to take precedence on the deformation process. The same tendency can be also seen for distribution of von Mises stress in the workpiece at maximum penetration. In the fully dynamic process the indenter decelerates to a complete stop before recoiling off the workpiece surface while in the other processes, the indenter experiences an increasing reaction force. In the area near the indenter tip and in the far-field, the distribution of von Mises stress for different modelling regimes have different characteristics defined by the competition between strain rate hardening and temperature softening in the Ti based alloy.

As the workpiece is work-hardened through penetration, it has a tendency to form a pile up with an associated indenter imprint in the workpiece. The pile-up height increases as friction at the workpiece-indenter interface decreases. It is also observed that the temperature distribution in the workpiece is highly localized (predominantly in a 0.1 mm layer near the indenter tip) and gets values in the range of 800˚C-1000˚C in dynamic analysis with relatively high indenter velocities and fully dynamic analysis as opposed to the static analysis and dynamic analysis with smaller inertial effects demonstrating moderate temperature changes.

The computational study presented in this paper demonstrates that there can be noticeable differences in the predicted values of deformation and stress-strain characteristics of the workpiece material depending on the chosen numerical modelling technique. The observed results qualitatively correlate to differences observed in experiments as well as in advanced machining processes. Thus, it becomes essential to define the process under study accurately before choosing a specific numerical modelling technique.

In the future we intend to quantitatively correlate our model to dynamic indentation experiments on Ti based alloys.

**Acknowledgement:** Authors would like to acknowledge Tõnu Leemet from Tampere University of Technology and Carsten Siemers from University of Technology Braunschweig for providing the material data for the Ti-based alloy. The research leading to these results has received funding from the European Union Seventh Framework Programme (FP7/2007-2013) under grant agreement No. PITN-GA-2008-211536, project MaMiNa.

## References

**Ahmed, N.; Mitrofanov, A. V.; Babitsky, V. I.; Silberschmidt, V. V.** (2006): Analysis of material response to ultrasonic vibration loading in turning Inconel 718. *Mater. Sci. Eng.*, vol. 424, pp. 318-325.

**Ahmed, N.; Mitrofanov, A. V.; Babitsky, V. I.; Silberschmidt, V. V.** (2007): Analysis of forces in ultrasonically assisted turning. *J. Sound Vibrat.* , vol. 308, pp. 845-854.

**Ahmed, N.; Mitrofanov, A. V.; Babitsky, V. I.; Silberschmidt, V. V.** (2007): 3D finite element analysis of ultrasonically assisted turning. *Comput. Mater. Sci.*, vol. 39, pp. 149-154.

**Ahmed, N.; Mitrofanov, A. V.; Babitsky, V. I.; Silberschmidt, V. V.** (2009): Enhanced finite element model of ultrasonically assisted turning. *Int. J. Machining Machinability Mater.*, vol. 6, pp. 159-173.

**Astashev, V. K.; Babitsky, V. I.** (1998): Ultrasonic cutting as a non-linear (vibro-impact) process. *Ultrasonics*, vol. 36, pp. 89–96.

**Babitsky, V. I.; Kalashnikov, A.; Meadows, A.; Wijesundara, A.** (2003): Ultrasonically assisted turning of aviation materials. *J. Mater. Process. Technol.*, vol. 132, pp. 157–167.

**Blumm, J.; Kaisersberger, E.** (2001): Accurate Measurement of Transformation Energetics and Specific Heat by DSC in the High-temperature Region. *J. Ther. Anal. Calor.*, vol. 64, pp. 385-391.

**Bocciarelli, M.; Maier, G.** (2007): Indentation and imprint mapping method for identification of residual stresses. *Comput. Mater. Sci.*, vol. 39, pp. 381-392.

**Davis, C. D.; Hunter, S. C.** (1960): Assessment of the strain rate sensitivity of metals by indentation with conical indenters, *J. Mech. Phys. Sol.*, vol. 8, pp. 235–254.

**Demiral, M.; Roy A.; Silberschmidt, V. V.** (2010): Repetitive indentation of Ti-based alloys: A numerical study. *IOP Conf. Series: Mater. Sci. Eng.*, vol. 10, 012105.

**Garrido Maneiro, M. A.; Rodriquez, J.** (2005): Pile-up effect on nanoindentation tests with spherical-conical tips. *Scripta Mater.*, vol. 52, pp. 593-598.

**Kolsky, H.** (1949): An investigation of the mechanical properties of materials at very high rates of loading, *Proc. R. Soc. London*, vol. 62, pp. 676–700.

**Li, Z.; Lambros, J.** (1999): Determination of the dynamic response of brittle composites by the use of the split Hopkinson pressure bar. *Compo. Sci. Technol.*, vol. 59, pp. 1097-1107.

**Lu, J.; Suresh S.; Ravichandrana, G.** (2003): Dynamic indentation for determining the strain rate sensitivity of metals. *J. Mech. Phys. Sol.*, vol. 51, pp. 1923-1938.

**Material property data** (2010): Temperature dependent thermal expansion coefficient for Ti based alloy (Ti15V3Cr3Al3Sn). Available at: www.matweb.com

**Maudlin, P.; Stout M.** (1996): Metal cutting simulation of 4340 steel using an accurate mechanical description of material strength and fracture. *Min. Met. Mat. Soc.*, pp. 29-41.

**Mitrofanov, A. V.; Ahmed, N.; Babitsky, V. I.; Silberschmidt, V. V.** (2005): Effect of lubrication and cutting paramters on ultrasonically assisted turning of Inconel 718. *J. Mater.Process. Technol*, vol. 162-163, pp. 649-654.

**Mok, C.H.; Duffy, J.** (1965): The dynamic stress–strain relation of metals as determined from impact tests with a hard ball. *Int. J. Mech. Sci.,* vol. 7, pp. 355–371.

**MSC, Marc User's Guide** (2005). MSC Software Corporation, Los Angeles.

**Nanoindenters** (2010): Tip geometries. Available at: http://www.microstartech.com/

**Ng, E-G.; El-Wardany, T.; Dumitrescu M.; Elbestawi M.** (2002): Physics-based simulation of high speed machining. *Mach. Sci. Technol.*, vol. 6, pp. 301-329.

**Suresh, S.; Giannakopoulos A. E.** (1998): A new method for estimating residual stresses by instrumented sharp indentation. *Acta Mater.*, vol. 46, pp. 5755-5767.

**Tabor, D.** (1950): *The hardness of metals*. Oxford: Clarendon Press.

**Tirupataiah, Y.; Sundararajan, G.** (1991): A dynamic indentation technique for the characterization of the high-strain rate plastic-flow behavior of ductile metals and alloys. *J. Mech. Phys. Solids*, vol. 39, pp. 243–271.